Structural and Multidisciplinary Optimization (2024) 67:46
https://doi.org/10.1007/s00158-024-03750-w

RESEARCH PAPER

Robust contact-constrained topology optimization considering uncertainty at the contact support

Timo Schmidt[1] · Benedikt Kriegesmann[2] · Robert Seifried[1]

Received: 16 August 2023 / Revised: 17 January 2024 / Accepted: 19 January 2024

Abstract
In this paper, the general framework for contact-constrained topology optimization of Strömberg and Klarbring (2010) is extended to robust topology optimization. In doing so, a linear elastic design domain is considered and the augmented Lagrangian approach is used to model the unilateral contact. For topology optimization, the design space is parametrized with the SIMP-approach and the Sigmund's filter is applied. Additionally, the robust framework considers uncertainties at the contact support such as deviations of the geometry of the contact surface and the friction coefficient. Both uncertainties are described by the first-order second-moment method which leads to minimal additional costs. In fact, only two additional linear equations must be solved to obtain the robust objective and its gradient with respect to the design variables. Having both the objective and the gradient, the design update is computed with the method of moving asymptotes. The robust framework is applied to 2D and 3D examples to prove its scalability for real-world applications.

Keywords Robust topology optimization · Robust design optimization · Contact · Method of moments

1 Introduction

Computer aided optimization has gained importance in recent years, however, it has still limitations in application. Besides other reasons, this is due to the fact, that optimizations are based on simulation models, which in turn are based on idealized model assumptions. It is well known, that the optimization algorithms exhaust the model assumptions to reduce the objective as much as possible. Due to that, it is of major importance to reduce the assumptions at crucial areas such as the force transmission zones. In order to weaken the model assumptions, Strömberg and Klarbring (2010) developed a framework for contact-constrained topology optimization. They concluded that standard boundary conditions might be well suited for finite element analysis but result in weak design concepts in topology optimization. Further analysis in Strömberg and Klarbring (2010) have revealed that optimized designs obtained by contact-constrained topology optimization are still very sensitive to the contact parameters. Therefore in this paper, the concepts of robust design optimization are derived as extension to the framework of Strömberg and Klarbring (2010).

The robust design optimization is motivated by poorly performing deterministically optimized designs, where neglected uncertainties are the reason for poor performance. For instance, the deterministic optimization is most likely based on ideal bearing assumptions and perfect loading. Moreover, tolerances of the geometry and the material are most often neglected as well. In consequence, the deterministic optimized design might not perform as expected. In topology optimization, the first steps towards robust design optimization were made in the field of reliability-based optimization with random loads, see Maute and Frangopol (2003); Jung and Cho (2004). Taking a closer look at random loads reveal, that one has typically only a few random parameters, so that Monte Carlo methods can be applied efficiently. More recently, also geometric uncertainties and spatially varying material parameters were examined, see Schevenels et al. (2011); Lazarov et al. (2012); Kriegesmann

Responsible Editor: W.H. Zhang

✉ Timo Schmidt
timo.schmidt@tuhh.de

[1] Institute of Mechanics and Ocean Engineering, Hamburg University of Technology, Eissendorfer Straße 42, Hamburg 21073, Hamburg, Germany

[2] Institute for Structural Mechanics in Lightweight Design, Hamburg University of Technology, Eissendorfer Straße 40, Hamburg 21073, Hamburg, Germany

Published online: 13 March 2024

and Lüdeker (2019). Here, robust design optimization problems such as the minimization of a weighted sum of mean and standard deviation of the objective function are mostly considered. Generally speaking, the number of random parameters increases significantly in comparison to random loads, so that Monte Carlo methods become very costly. Thus, several hundreds to thousands of random Monte Carlo samples must be computed in each iteration of the optimization to achieve a good estimate of the influence of the modeled uncertainty. To avoid these tremendous computational costs, other methods such as the non-intrusive polynomial chaos expansion, see Keshavarzzadeh et al. (2017), and the first-order second-moment method, see Kriegesmann and Lüdeker (2019), were successfully applied to topology optimization. The latter uses a first-order Taylor series expansion of the objective function to approximate the first two stochastic moments, namely the mean and the variance.

This work combines the contact-constrained topology optimization with the robust design optimization. The first-order second-moment method is used to approximate both, the influence of scattering contact geometries and friction coefficients, which leads to adaptions in the optimized designs.

2 Equilibrium equations of the contact problem

The equilibrium equations of a linear elastic body in contact are here based on the finite element method. In doing so, the stiffness matrix $\boldsymbol{K}$, the nodal displacement field $\boldsymbol{d}$, the nodal contact forces $\boldsymbol{f}_{\text{con}}$ and the external forces $\boldsymbol{q}$ are introduced. Additionally, the modified SIMP approach Sigmund (2007) is used. Hence, the Young's modulus E_i of each element is a function of its normalized density $\varphi_i \in [0, 1]$

$$E_i = E_{\min} + \varphi_i^p (E_{\max} - E_{\min}). \tag{1}$$

Here, the penalization factor $p = 3$ is chosen. The Young's modulus of the void is defined as $E_{\min}$ and the modulus of the material is $E_{\max}$. Further, the normalized densities are the design variables of the later defined optimization problem, which are summarized in the vector $\boldsymbol{\varphi}$. Hence, the stiffness matrix depends on the element's density and the equilibrium equations are

$$\boldsymbol{K}(\boldsymbol{\varphi})\boldsymbol{d} + \boldsymbol{f}_{\text{con}} - \boldsymbol{q} = \boldsymbol{0}, \tag{2}$$

which have to be amended by the contact conditions in order to compute the contact forces $\boldsymbol{f}_{\text{con}}$.

2.1 Normal contact condition

Fig. 1 illustrates a potential contact node A of a linear elastic body. Here, the contact gap is defined as

$$\eta^A = g^A - \boldsymbol{n}^A \cdot \boldsymbol{d}^A, \tag{3}$$

where the contact normal is $\boldsymbol{n}^A$ and g^A is the initial gap between the undeformed configuration and the support.

In order to solve Eq. (2), the nodal contact forces $\boldsymbol{f}_{\text{con}}$ must be computed. Therefore, Signorini's contact conditions (1959) are introduced. The conditions for the A-th contact node read

$$\xi^A \geq 0, \quad \eta^A \geq 0, \quad \xi^A \eta^A = 0. \tag{4}$$

The contact conditions of Eq. (4) state, that there is either a gap $\eta^A > 0$ between the $A - th$ node and the contact support and thus no contact force is transmitted $\xi^A = 0$ nor that the node is in contact with the support $\eta^A = 0$ and a contact force $\xi^A > 0$ is transmitted. In practice, Signorini's contact conditions are imposed by functions that are either non-smooth or have a singularity at zero. The used contact function is

$$\Phi^A = -\xi^A + \max(0, \xi^A - \eta^A) = 0. \tag{5}$$

Inserting Eq. (3) into the contact function of Eq. (5) results in

$$\Phi^A = -\xi^A + \max(0, \xi^A - r(g^A - \boldsymbol{n}^A \cdot \boldsymbol{d}^A)) = 0, \tag{6}$$

where $r > 0$ is a factor introduced to increase the numerical performance. Eq. (6) is the standard augmented Lagrangian formulation of Signorini's contact conditions. This was compared to an approach of Facchinei et al. (1999) in Strömberg and Klarbring (2010). It was concluded in Strömberg and

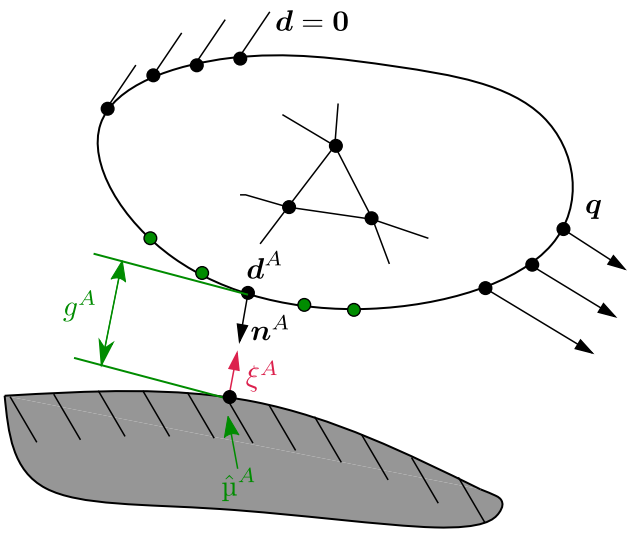

Fig. 1 A linear elastic body unilaterally constrained by a rigid support Strömberg and Klarbring (2010)

Klarbring (2010) that the augmented Lagrangian approach was slightly better than the approach of Facchinei et al. (1999). Additionally, the nodal contact force $\boldsymbol{f}_{\text{con}}$ of Eq. (2) are

$$\boldsymbol{f}_{\text{con}} = \boldsymbol{N}^{\text{T}}\boldsymbol{\xi}, \tag{7}$$

where $\boldsymbol{\xi}$ is the normal contact force vector of all contact nodes and the matrix $\boldsymbol{N}$ maps the contact force vector into the nodal domain. Therefore, $\boldsymbol{N}$ consists of all contact normal directions $\boldsymbol{n}^A$. It is assumed that the normal directions do not change due to the displacement field, since only small displacements are considered.

Here, the equilibrium equations considering only unilateral-normal contact forces read

$$\hat{\boldsymbol{h}}_{\text{c}}(\boldsymbol{d}, \boldsymbol{\xi}, \boldsymbol{\varphi}) = \begin{Bmatrix} \boldsymbol{K}(\boldsymbol{\varphi})\boldsymbol{d} + \boldsymbol{f}_{\text{con}}(\boldsymbol{\xi}) - \boldsymbol{q} \\ \boldsymbol{\Phi}(\boldsymbol{d}, \boldsymbol{\xi}) \end{Bmatrix} = \boldsymbol{0}, \tag{8}$$

and can be linearized to

$$\hat{\boldsymbol{h}}_{\text{c}}(\boldsymbol{x}, \boldsymbol{\varphi}) = \underbrace{\begin{bmatrix} \boldsymbol{K}(\boldsymbol{\varphi}) & \boldsymbol{N}^{\text{T}} \\ \dfrac{\partial \boldsymbol{\Phi}(\boldsymbol{x})}{\partial \boldsymbol{d}} & \dfrac{\partial \boldsymbol{\Phi}(\boldsymbol{x})}{\partial \boldsymbol{\xi}} \end{bmatrix}}_{\hat{\boldsymbol{J}}_{\text{c}}} \underbrace{\begin{bmatrix} \boldsymbol{d} \\ \boldsymbol{\xi} \end{bmatrix}}_{\boldsymbol{x}} - \underbrace{\begin{bmatrix} \boldsymbol{q} \\ \boldsymbol{\Phi}_{\text{c}} \end{bmatrix}}_{\boldsymbol{r}_{\text{c}}} = \boldsymbol{0}, \tag{9}$$

where the contact Jacobian $\hat{\boldsymbol{J}}_{\text{c}}$, the state vector $\boldsymbol{x}$ and the state independent vector $\boldsymbol{r}_{\text{c}}$ are introduced. The vector $\boldsymbol{r}_{\text{c}}$ consists of the external forces $\boldsymbol{q}$ and the state independent part of the contact law. The non-smoothness of the Karush-Kuhn-Tucker Eq. (9) result from the used contact law or respectively from the lower rows of the Jacobian, since they depend on the current state of the contact nodes. Hence, one has to distinguish between nodes that are in contact and nodes that are not in contact. The A-th contact node is in contact, if

$$\xi^A - r(g^A - \boldsymbol{n}^A \cdot \boldsymbol{d}^A) \geq 0. \tag{10}$$

Consequentially, the partial derivatives of the contact condition inside the Jacobian read

$$\frac{\partial \Phi^A}{\partial \boldsymbol{d}^A} = \begin{cases} 0 & \text{no contact} \\ r\boldsymbol{n}^A & \text{in contact} \end{cases}, \tag{11}$$

$$\frac{\partial \Phi^A}{\partial \xi^A} = \begin{cases} -1 & \text{no contact} \\ 0 & \text{in contact} \end{cases} \tag{12}$$

and the right-hand side is

$$\Phi_{\text{c}}^A = \begin{cases} 0 & \text{no contact} \\ rg^A & \text{in contact} \end{cases}. \tag{13}$$

In doing so, a non-linear solver such as a line-search algorithm can be used to calculate the solution of displacement field $\boldsymbol{d}$ and the contact forces $\boldsymbol{\xi}$ Strömberg and Klarbring (2010). Given a density distribution $\tilde{\boldsymbol{\varphi}}$ and a guess for the state vector $\tilde{\boldsymbol{x}}$, the search direction of the line-search algorithm is

$$\boldsymbol{s} = \left(\boldsymbol{J}_{\text{c}}(\tilde{\boldsymbol{x}}, \tilde{\boldsymbol{\varphi}})\right)^{-1} \boldsymbol{h}(\tilde{\boldsymbol{x}}, \tilde{\boldsymbol{\varphi}}). \tag{14}$$

2.2 Tangential contact condition

In this work, friction is modeled as global sliding. Using global sliding is motivated by a footnote in Strömberg and Klarbring (2010). In contrast to other laws such as Coulombs-Law, the influence of random friction coefficients can be captured by the used first-order second-moment method, if global sliding is considered. This is due to the fact, that the first-order second-moment method needs the derivative of the objective with respect to the random variable. In consequence, the friction coefficient must occur explicitly in the equilibrium equations, see Schmidt et al. (2022).

In doing so, the contact forces taking friction into account read

$$\boldsymbol{f}_{\text{con}} = (\boldsymbol{N} + \hat{\mu}\boldsymbol{T})^{\text{T}}\boldsymbol{\xi}, \tag{15}$$

where no additional tangential contact function is introduced. Here, $\boldsymbol{N}$ holds the normal directions, $\boldsymbol{T}$ the tangential directions and $\boldsymbol{\xi}$ are the normal contact forces. In consequence, the tangential contact forces are always proportional to the normal contact forces.

The linear momentum of Eq. (2) and the contact functions of all contact nodes $\boldsymbol{\Phi} \in \mathbb{R}^{n_{\text{con}}}$ defined in Eq. (6) form the non-linear equilibrium equations. They read

$$\boldsymbol{h}_{\text{c}}(\boldsymbol{d}, \boldsymbol{\xi}, \boldsymbol{\varphi}) = \begin{Bmatrix} \boldsymbol{K}(\boldsymbol{\varphi})\boldsymbol{d} + \boldsymbol{f}_{\text{con}}(\boldsymbol{\xi}) - \boldsymbol{q} \\ \boldsymbol{\Phi}(\boldsymbol{d}, \boldsymbol{\xi}) \end{Bmatrix} = \boldsymbol{0}, \tag{16}$$

$$\begin{aligned} \boldsymbol{h}_{\text{c}}(\boldsymbol{x}, \boldsymbol{\varphi}) = & \underbrace{\begin{bmatrix} \boldsymbol{K}(\boldsymbol{\varphi}) & (\boldsymbol{N} + \hat{\mu}\boldsymbol{T})^{\text{T}} \\ \dfrac{\partial \boldsymbol{\Phi}(\boldsymbol{x})}{\partial \boldsymbol{d}} & \dfrac{\partial \boldsymbol{\Phi}(\boldsymbol{x})}{\partial \boldsymbol{\xi}} \end{bmatrix}}_{\boldsymbol{J}_{\text{c}}} \underbrace{\begin{bmatrix} \boldsymbol{d} \\ \boldsymbol{\xi} \end{bmatrix}}_{\boldsymbol{x}} \\ & \cdots - \underbrace{\begin{bmatrix} \boldsymbol{q} \\ \boldsymbol{\Phi}_{\text{c}}(\boldsymbol{x}) \end{bmatrix}}_{\boldsymbol{r}_{\text{c}}} = \boldsymbol{0}, \end{aligned} \tag{17}$$

where the partial derivatives of the normal contact laws of Eqs. (12) and (13) are unchanged. Eq. (17) forms the basis for the robust topology optimization approach.

3 Robust topology optimization

The goal of robust topology optimization is to consider defined unknown or stochastically scattered parameters during the optimization process to obtain a less sensitive optimized design. The work of Zang et al. (2022) provides an overview of the main concepts of robust design optimization.

In contrast to the deterministic optimization problem, the robust optimization problem minimizes a weighted sum of the mean μ_f and the standard deviation σ_f of the deterministic objective $f(\boldsymbol{y}, \boldsymbol{z})$. In doing so, the objective f depends on the design variables $\boldsymbol{y}$ and the random vector $\boldsymbol{z}$, which describes the considered uncertainty. Thus, the robust optimization problem is

$$\min_{\boldsymbol{y}} \mu_f(\boldsymbol{y}) + \kappa\sigma_f(\boldsymbol{y}), \quad \text{s.t.} \begin{cases} \boldsymbol{g}(\boldsymbol{y}) \leq \boldsymbol{0} \\ \boldsymbol{h}(\boldsymbol{y}) = \boldsymbol{0} \end{cases} \tag{18}$$

where the weighting factor $\kappa > 0$ of the mean and the standard deviation is introduced. Furthermore, the optimization is subjection to inequality constraints $\boldsymbol{g}$ and equality constraints $\boldsymbol{h}$. Hence, in order to apply robust topology optimization, the mean $\mu_f(\boldsymbol{y})$ and the standard deviation $\sigma_f(\boldsymbol{y})$ or the variance $\sigma_f(\boldsymbol{y})^2$ of the objective f must be computed. In general, the mean of the objective is defined as

$$\mu_f = \int_{-\infty}^{\infty} f(z)p(z)dz, \tag{19}$$

and the variance is defined as

$$\sigma_f^2 = \int_{-\infty}^{\infty} (f(z) - \mu_f)^2 p(z)dz, \tag{20}$$

where $p(z)$ is a defined probability density function.

If the evaluation of the objective f of the optimization can be done very fast, Monte Carlo simulations can be used to approximate both by

$$\mu_f(\boldsymbol{y}) \approx \sum_{i=1}^{n_{\text{MCS}}} f(z_i) \tag{21}$$

and

$$\sigma_f^2 \approx \frac{1}{n_{\text{MCS}} - 1} \sum_{i=1}^{n_{\text{MCS}}} (f(z_i) - \mu_f)^2. \tag{22}$$

Here z_i is a set of randomly sampled variables and n_{MCS} is the total number of Monte Carlo samples. However, computing the objective in structural mechanics is computationally costly, especially if contact is considered. Therefore, Monte Carlo simulation can often only be used as benchmark to analyze the accuracy of other approximations of the mean and the variance.

One alternative way to approximate mean and variance is based on a Taylor series expansion of the objective function, which is sometimes referred to as Method of Moments, see Papoutsis-Kiachagias et al. (2012). Here, the linear approximation, namely the first-order second-moment method (FOSM) is applied. It was introduced by Cornell (1969) and successfully applied to topology optimization by Kriegesmann and Lüdeker (2019). In doing so, the mean is approximated by

$$\mu_f \approx f(\boldsymbol{\mu}_z), \tag{23}$$

where the mean of the random vector $\boldsymbol{z}$ is $\boldsymbol{\mu}_z$. Further, the variance is approximately

$$\sigma_f^2 \approx \sum_{i=1}^{n} \sum_{j=1}^{n} \frac{\partial f(\boldsymbol{\mu}_z)}{\partial z_i} \frac{\partial f(\boldsymbol{\mu}_z)}{\partial z_j} \text{cov}(z_i, z_j). \tag{24}$$

The number of random quantities is n and $\text{cov}(z_i, z_j)$ is an entry of the covariance matrix, see Kriegesmann and Lüdeker (2019); Haldar and Mahadevan (1999).

4 Robust contact-constrained compliance optimization

In this work, the compliance of a linear-elastic structure in unilateral contact with a support should be minimized. The compliance reads

$$c = \boldsymbol{q}^T \boldsymbol{d} = \begin{bmatrix} \boldsymbol{q} \\ \boldsymbol{0} \end{bmatrix}^{\text{T}} \begin{bmatrix} \boldsymbol{d} \\ \boldsymbol{\xi} \end{bmatrix} = \boldsymbol{r}^{\text{T}} \boldsymbol{x}, \tag{25}$$

where $\boldsymbol{x}$ is the solution of the contact problem of Eq. (17). The design variables of the optimization are the normalized densities $\boldsymbol{y} = \boldsymbol{\varphi}$ of the finite element discretization. Additionally, the geometry and the local friction coefficients of the support are considered to be random. The described setup is shown in Fig. 2, where the surface of the support structure scatters due to, e.g., manufacturing tolerances. More precisely, the actual gap g^A between the A-th contact node and the support structure as well as the actual nodal friction coefficient $\hat{\mu}^A$ are assumed to be random. Hence, the random vector is

$$\boldsymbol{z} = \begin{bmatrix} \boldsymbol{z}_{\text{g}} \\ \boldsymbol{z}_{\hat{\mu}} \end{bmatrix} \in \mathbb{R}^{2n_{\text{con}}}, \tag{26}$$

where the subvector $\boldsymbol{z}_{\text{g}} = [z_{\text{g}}^1, \ldots, z_{\text{g}}^{n_{\text{con}}}]^{\text{T}}$ holds all random gaps and $\boldsymbol{z}_{\hat{\mu}} = [z_{\hat{\mu}}^1, \ldots, z_{\hat{\mu}}^{n_{\text{con}}}]^{\text{T}}$ holds all random friction coefficients of all contact nodes. The expected shape of the

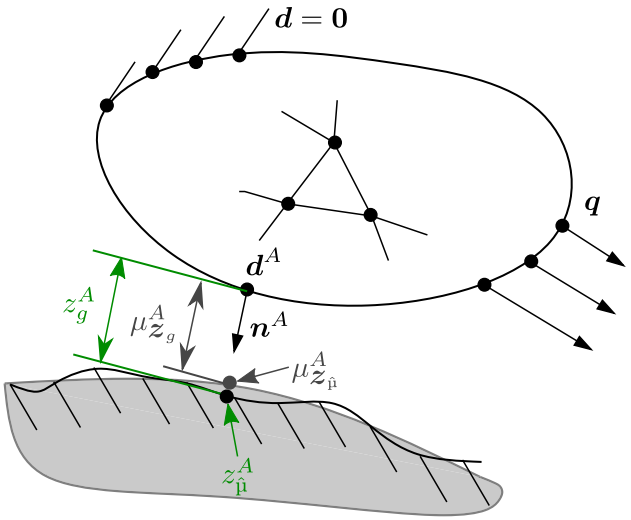

Fig. 2 A linear elastic body unilaterally constrained by a non-ideal rigid support (z_{g}^A - random contact gap, $\mu_{z_{\mathrm{g}}}^A$ - mean of the random contact gap, $z_{\hat{\mu}}^A$ - random friction coefficient, $\mu_{z_{\hat{\mu}}}^A$ - mean of the random friction coefficient)

support is shown in gray in Fig. 2 and locally described by the mean values $\mu_{z_{\mathrm{g}}}^A$ and $\mu_{z_{\hat{\mu}}}^A$ of the random variables $\boldsymbol{z}_{\mathrm{g}}$ and $\boldsymbol{z}_{\hat{\mu}}$. Please note that $\hat{\mu}$ is the friction coefficient, whereas μ is the mean.

The resulting robust optimization problem reads

$$\min_{\boldsymbol{\varphi}} \mu_c(\boldsymbol{\varphi}) + \kappa\sigma_c(\boldsymbol{\varphi}) \quad \text{s.t.} \begin{cases} \boldsymbol{h}_{\mathrm{c}}(\boldsymbol{\varphi}, \boldsymbol{x}) = \mathbf{0}, \\ V(\boldsymbol{\varphi}) - V_0 \leq 0, \\ \mathbf{0} \leq \boldsymbol{\varphi} \leq \mathbf{1}. \end{cases} \tag{27}$$

The equilibrium equations of the contact problem $\boldsymbol{h}_{\mathrm{c}}$, a volume constraints as well as the constraint on the design variables must be fulfilled.

Last, the scattering of the random variables must be defined. The random variables $\boldsymbol{z}_{\mathrm{g}}$ and $\boldsymbol{z}_{\hat{\mu}}$ are assumed to be independent. However, they are assumed to scatter spatially. Their random field is chosen to be stationary and homogeneous. In doing so, the exponential correlation function for the contact nodes i and j is

$$C_{i,j} = \exp\left(-\frac{||\boldsymbol{d}^i - \boldsymbol{d}^j||^2}{l_c^2}\right), \tag{28}$$

where l_c is the correlation length. If the standard deviation of the random variables $\sigma(\boldsymbol{z})$ is given, the covariance is

$$\mathrm{cov}(z_i, z_j) = C_{i,j}\sigma(z_i)\sigma(z_j), \tag{29}$$

and the covariance $\mathrm{cov}(z_i, z_j)$ is stored in the covariance matrix $\boldsymbol{\Sigma}_{\boldsymbol{z}}$.

Note that, the scattering of the random gap z_{g}^A and the friction coefficient $z_{\hat{\mu}}^A$ of the A-th node are independent of each other. However, the gaps and the friction coefficients are correlated to their neighbor gaps and friction coefficients by the correlation function.

4.1 Objective

In contrast to the standard compliance optimization, the robust compliance optimization problem consists of the mean and the standard deviation of the compliance. In consequence, both must be computed and the mean of the compliance is approximated using FOSM

$$\mu_c(\boldsymbol{\varphi}) \approx c(\boldsymbol{x}(\boldsymbol{\varphi}), \boldsymbol{\mu}_z). \tag{30}$$

Thus, the mean is approximated by the standard compliance.

However, the standard deviation is based on the variance approximation of Eq. (24), where the costly partial derivative of the compliance with respect to the random variables $\dfrac{\partial c(\boldsymbol{\mu}_z)}{\partial \boldsymbol{z}}$ is needed. In order to compute the gradient with respect to the random friction coefficients $z_{\hat{\mu}}^A$, the equilibrium equations must explicitly depend on the friction coefficients. This is guaranteed using the global sliding friction model introduced in Eq. (17).

The numerical costs can be reduced to a minimum by introducing the arbitrary adjoint variable $\boldsymbol{\zeta}$. The adjoint variable is multiplied by the equilibrium equations $\boldsymbol{h}_{\mathrm{c}}(\boldsymbol{x}(\boldsymbol{\mu}_z)) = \mathbf{0}$, so that it can be arbitrary chosen. The compliance evaluated at the mean of the random vector is then

$$c(\boldsymbol{x}, \boldsymbol{\mu}_z) = \boldsymbol{r}^{\mathrm{T}}\boldsymbol{x}(\boldsymbol{\mu}_z) - \boldsymbol{\zeta}^{\mathrm{T}}\boldsymbol{h}_{\mathrm{c}}(\boldsymbol{x}(\boldsymbol{\mu}_z)), \tag{31}$$

and its derivative with respect to the random variable z_i reads

$$\begin{aligned} \frac{\partial c(\boldsymbol{x}, \boldsymbol{\mu}_z)}{\partial z_i} &= \underbrace{\frac{\partial \boldsymbol{r}}{\partial z_i}^{\mathrm{T}}}_{\mathbf{0}}\boldsymbol{x}(\boldsymbol{\mu}_z) + \boldsymbol{r}^{\mathrm{T}}\frac{\partial \boldsymbol{x}(\boldsymbol{\mu}_z)}{\partial z_i} - \boldsymbol{\zeta}_i^{\mathrm{T}}\frac{\partial \boldsymbol{h}_{\mathrm{c}}(\boldsymbol{x}(\boldsymbol{\mu}_z))}{\partial z_i} \\ &= \boldsymbol{r}^{\mathrm{T}}\frac{\partial \boldsymbol{x}(\boldsymbol{\mu}_z)}{\partial z_i} - \boldsymbol{\zeta}_i^{\mathrm{T}}\frac{\partial \boldsymbol{J}_{\mathrm{c}}(\boldsymbol{x}(\boldsymbol{\mu}_z))}{\partial z_i}\boldsymbol{x}(\boldsymbol{\mu}_z) \\ &\quad \cdots - \boldsymbol{\zeta}_i^{\mathrm{T}}\boldsymbol{J}_{\mathrm{c}}(\boldsymbol{x}(\boldsymbol{\mu}_z))\frac{\partial \boldsymbol{x}(\boldsymbol{\mu}_z)}{\partial z_i} + \boldsymbol{\zeta}_i^{\mathrm{T}}\frac{\partial \boldsymbol{r}_{\mathrm{c}}(\boldsymbol{\mu}_z)}{\partial z_i} \\ &= \left(\boldsymbol{r}^{\mathrm{T}} - \boldsymbol{\zeta}_i^{\mathrm{T}}\boldsymbol{J}_{\mathrm{c}}(\boldsymbol{x}(\boldsymbol{\mu}_z))\right)\frac{\partial \boldsymbol{x}(\boldsymbol{\mu}_z)}{\partial z_i} - \boldsymbol{\zeta}_i^{\mathrm{T}} \\ &\quad \cdots \left(\frac{\partial \boldsymbol{J}_{\mathrm{c}}(\boldsymbol{x}(\boldsymbol{\mu}_z))}{\partial z_i}\boldsymbol{x}(\boldsymbol{\mu}_z) - \frac{\partial \boldsymbol{r}_{\mathrm{c}}(\boldsymbol{\mu}_z)}{\partial z_i}\right). \end{aligned} \tag{32}$$

If the adjoint $\boldsymbol{\zeta}$ is chosen as

$$\left(\boldsymbol{r}^{\mathrm{T}} - \boldsymbol{\zeta}_i^{\mathrm{T}}\boldsymbol{J}_{\mathrm{c}}(\boldsymbol{x}(\boldsymbol{\mu}_z))\right) = \mathbf{0}, \tag{33}$$

the derivative of the compliance with respect to the random variables simplifies to

$$\frac{\partial c(\boldsymbol{x},\boldsymbol{\mu}_z)}{\partial z_i} = -\boldsymbol{\zeta}^{\mathrm{T}}\left(\frac{\partial \boldsymbol{J}_{\mathrm{c}}(\boldsymbol{x}(\boldsymbol{\mu}_z))}{\partial z_i}\boldsymbol{x}(\boldsymbol{\mu}_z) - \frac{\partial \boldsymbol{r}_{\mathrm{c}}(\boldsymbol{\mu}_z)}{\partial z_i}\right), \tag{34}$$

where the adjoint Eq. (33) is independent of the random variables z_i. Consequentially, the adjoint is the same for all partial derivatives of $\boldsymbol{z}$. Hence, the adjoint $\boldsymbol{\zeta} = \boldsymbol{\zeta}_i$ is just calculated once. Next to that, the partial derivatives of the Jacobian with respect to the A-th contact node are

$$\frac{\partial \boldsymbol{J}_{\mathrm{c}}(\boldsymbol{x}(\boldsymbol{\mu}_z))}{\partial z^i_{\mathrm{g}}} = \begin{bmatrix} \boldsymbol{0} & \boldsymbol{0} \\ \boldsymbol{0} & \boldsymbol{0} \end{bmatrix} \tag{35}$$

and

$$\frac{\partial \boldsymbol{J}_{\mathrm{c}}(\boldsymbol{x}(\boldsymbol{\mu}_z))}{\partial z^i_{\mu}} = \begin{bmatrix} \boldsymbol{0} & \begin{Bmatrix} \boldsymbol{0}, & i \neq A \\ (\boldsymbol{t}^A)^{\mathrm{T}}, & i = A \end{Bmatrix} \\ \boldsymbol{0} & \boldsymbol{0} \end{bmatrix}. \tag{36}$$

The derivatives of $\boldsymbol{r}_{\mathrm{c}}(\boldsymbol{\mu}_z)$ are

$$\frac{\partial \boldsymbol{r}_{\mathrm{c}}(\boldsymbol{\mu}_z)}{\partial z^i_{\mathrm{g}}} = \begin{bmatrix} \boldsymbol{0} \\ \begin{Bmatrix} 0, & i \neq A \\ r, & i = A \,\&\, \eta^A \leq 0 \end{Bmatrix} \end{bmatrix} \tag{37}$$

and

$$\frac{\partial \boldsymbol{r}_{\mathrm{c}}(\boldsymbol{\mu}_z)}{\partial z^i_{\mu}} = \begin{bmatrix} \boldsymbol{0} \\ \boldsymbol{0} \end{bmatrix}. \tag{38}$$

The results of Eqs. (35)–(38) imply that one partial derivative of Eq. (34) is zero, since z_i corresponds to either a random gap z^i_{g} or a random friction coefficient $z^i_{\hat{\mu}}$. If the considered randomness corresponds to a contact gap, the partial derivative of the compliance is

$$\frac{\partial c(\boldsymbol{x},\boldsymbol{\mu}_z)}{\partial z^i_{\mathrm{g}}} = \boldsymbol{\zeta}\frac{\partial \boldsymbol{r}_{\mathrm{c}}(\boldsymbol{\mu}_z)}{\partial z^i_{\mathrm{g}}}, \tag{39}$$

otherwise a random friction coefficient is considered, where the partial derivative is

$$\frac{\partial c(\boldsymbol{x},\boldsymbol{\mu}_z)}{\partial z^i_{\mu}} = -\boldsymbol{\zeta}\frac{\partial \boldsymbol{J}_{\mathrm{c}}(\boldsymbol{x}(\boldsymbol{\mu}_z))}{\partial z^i_{\mu}}\boldsymbol{x}(\boldsymbol{\mu}_z). \tag{40}$$

In both cases, the adjoint $\boldsymbol{\zeta}$ is defined by the same adjoint Eq. (33). As a result, only one additional set of linear equations must be solved to calculate the FOSM approximation of the variance of the compliance.

Next, the variance is calculated as stated in Eq. (24) and the objective of the defined optimization problem Eq. (27) is approximated with FOSM. The optimization problem using FOSM reads

$$\begin{aligned} \min_{\boldsymbol{\varphi}} \; & \underbrace{c(\boldsymbol{x},\boldsymbol{\mu}_z)}_{\mu_c^{\mathrm{FOSM}}} + \kappa \\ & \cdots \underbrace{\sqrt{\sum_{i=1}^{2n_{\mathrm{con}}}\sum_{j=1}^{2n_{\mathrm{con}}}\frac{\partial c(\boldsymbol{x},\boldsymbol{\mu}_z)}{\partial z_i}\frac{\partial c(\boldsymbol{x},\boldsymbol{\mu}_z)}{\partial z_j}\mathrm{cov}(z_i,z_j)}}_{\sigma_c^{\mathrm{FOSM}}} \\ \text{s.t.} \; & \begin{cases} \boldsymbol{h}_{\mathrm{c}}(\boldsymbol{\varphi},\boldsymbol{x}) = \boldsymbol{0}, \\ V(\boldsymbol{\varphi}) - V_0 \leq 0, \\ \boldsymbol{0} \leq \boldsymbol{\varphi} \leq \boldsymbol{1}, \end{cases} \end{aligned} \tag{41}$$

where $\dfrac{\partial c(\boldsymbol{x},\boldsymbol{\mu}_z)}{\partial z_i}$ is defined by Eqs. (39) and (40) and the covariance is obtained from the covariance matrix

$$\boldsymbol{\Sigma}_z = \begin{bmatrix} \boldsymbol{\Sigma}_{z_{\mathrm{g}}} & \boldsymbol{0} \\ \boldsymbol{0} & \boldsymbol{\Sigma}_{z_{\mu}} \end{bmatrix}. \tag{42}$$

In Eq. (41) κ is a weighting factor between the mean and the standard deviation of the objective. If $\kappa = 0$, the robust optimization problem simplifies to the non-robust contact-constrained topology optimization problem of Strömberg and Klarbring (2010).

4.2 Gradient of the objective using first-order second-moment

The topology optimization update inside the used optimization algorithm is computed with the method of moving asymptotes, see Svanberg (1987). In doing so, the derivative of the objective with respect to the design variables is necessary. The gradient of the variance approximated by FOSM can either be calculated using the adjoint method, see Kranz et al. (2023) or by the non-intrusive approaches presented in Steltner et al. (2022) or Krüger et al. (2023). Though a non-intrusive approach is appealing and the one given by Krüger et al. (2023) only requires one additional objective function evaluation per iteration, it was shown in Krüger et al. (2023) that this approach is not well suited for contact problems due to the discontinuity induced by the contact. Hence, the adjoint method is used, which requires a case-dependent derivation of the governing equation. In the following, this derivation is given for both addends of the objective Eq. (41).

The first addend of Eq. (41) is the approximation of the mean of the compliance and an adjoint equation is used once again to compute this gradient. Thus, the compliance is extended to

$$\tilde{c}(\boldsymbol{x},\boldsymbol{\mu}_z) = \mu_c^{\mathrm{FOSM}} - \tilde{\boldsymbol{\zeta}}^{\mathrm{T}}\boldsymbol{h}_{\mathrm{c}}(\boldsymbol{x},\boldsymbol{\mu}_z), \tag{43}$$

where the same adjoint approach is used as for the computation of the variance

$$\begin{aligned}\frac{\partial \tilde{c}(\boldsymbol{x},\boldsymbol{\mu}_z)}{\partial \varphi_e} &= \frac{\partial \boldsymbol{r}}{\partial \varphi_e}^{\mathrm{T}} \boldsymbol{x}(\boldsymbol{\mu}_z) + \boldsymbol{r}^{\mathrm{T}} \frac{\partial \boldsymbol{x}(\boldsymbol{\mu}_z)}{\partial \varphi_e} \\ &\quad \dots - \tilde{\boldsymbol{\zeta}}^{\mathrm{T}} \frac{\partial \boldsymbol{h}_{\mathrm{c}}(\boldsymbol{x},\boldsymbol{\mu}_z)}{\partial \varphi_e} \\ &= \boldsymbol{r}^{\mathrm{T}} \frac{\partial \boldsymbol{x}(\boldsymbol{\mu}_z)}{\partial \varphi_e} - \tilde{\boldsymbol{\zeta}}^{\mathrm{T}} \frac{\partial \boldsymbol{J}_{\mathrm{c}}(\boldsymbol{x}(\boldsymbol{\mu}_z))}{\partial \varphi_e} \boldsymbol{x}(\boldsymbol{\mu}_z) \\ &\quad \dots - \tilde{\boldsymbol{\zeta}}^{\mathrm{T}} \boldsymbol{J}_{\mathrm{c}}(\boldsymbol{x}(\boldsymbol{\mu}_z)) \frac{\partial \boldsymbol{x}(\boldsymbol{\mu}_z)}{\partial \varphi_e} + \tilde{\boldsymbol{\zeta}}^{\mathrm{T}} \frac{\partial \boldsymbol{r}_{\mathrm{c}}(\boldsymbol{\mu}_z)}{\partial \varphi_e} \\ &= \left(\boldsymbol{r}^{\mathrm{T}} - \tilde{\boldsymbol{\zeta}}^{\mathrm{T}} \boldsymbol{J}_{\mathrm{c}}(\boldsymbol{x}(\boldsymbol{\mu}_z))\right) \frac{\partial \boldsymbol{x}(\boldsymbol{\mu}_z)}{\partial \varphi_e} - \tilde{\boldsymbol{\zeta}}^{\mathrm{T}} \\ &\quad \dots \left(\frac{\partial \boldsymbol{J}_{\mathrm{c}}(\boldsymbol{x}(\boldsymbol{\mu}_z))}{\partial \varphi_e} \boldsymbol{x}(\boldsymbol{\mu}_z) - \frac{\partial \boldsymbol{r}_{\mathrm{c}}(\boldsymbol{\mu}_z)}{\partial \varphi_e} \right).\end{aligned} \tag{44}$$

It turns out, that the same adjoint system of equations known from Eq. (33) must be solved to avoid computing the costly derivative $\frac{\partial \boldsymbol{x}(\boldsymbol{\mu}_z)}{\partial \varphi_e}$. In consequence, the adjoint is $\tilde{\boldsymbol{\zeta}} = \boldsymbol{\zeta}$, if the adjoint equation is chosen such that

$$\left(\boldsymbol{r}^{\mathrm{T}} - \tilde{\boldsymbol{\zeta}}^{\mathrm{T}} \boldsymbol{J}_{\mathrm{c}}(\boldsymbol{x}(\boldsymbol{\mu}_z))\right) = \boldsymbol{0}. \tag{45}$$

Thus, no further computational costs occur for the first addend of the derivative. The derivative is

$$\frac{\partial \tilde{c}(\boldsymbol{x},\boldsymbol{\mu}_z)}{\partial \varphi_e} = -\boldsymbol{\zeta}^{\mathrm{T}} \left(\frac{\partial \boldsymbol{J}_{\mathrm{c}}(\boldsymbol{x}(\boldsymbol{\mu}_z))}{\partial \varphi_e} \boldsymbol{x}(\boldsymbol{\mu}_z) \right). \tag{46}$$

The derivative of the Jacobian with respect to the element's density is

$$\frac{\partial \boldsymbol{J}_{\mathrm{c}}(\boldsymbol{x}(\boldsymbol{\mu}_z))}{\partial \varphi_e} = \begin{bmatrix} \frac{\partial \boldsymbol{K}(\boldsymbol{\varphi})}{\partial \varphi_e} & \boldsymbol{0} \\ \boldsymbol{0} & \boldsymbol{0} \end{bmatrix}, \tag{47}$$

where the derivative of the stiffness matrix with respect to the e-th element is the derivative of the element's local stiffness matrix, including the SIMP approach of Eq. (1). A more detailed derivation can be found in Strömberg and Klarbring (2010).

Coming to the second addend of the objective, the derivative of $\sigma_{\mathrm{c}}^{\mathrm{FOSM}}$ with respect to the elements densities must be computed as well. Consequentially, it is necessary to compute

$$\begin{aligned}\frac{\partial \sigma_{\mathrm{c}}^{\mathrm{FOSM}}}{\partial \varphi_e} &= \frac{1}{2\sigma_{\mathrm{c}}^{\mathrm{FOSM}}} \frac{\partial}{\partial \varphi_e} \left(\sum_{i=1}^{2n_{\mathrm{con}}} \sum_{j=1}^{2n_{\mathrm{con}}} \frac{\partial c(\boldsymbol{x},\boldsymbol{\mu}_z)}{\partial z_i} \right. \\ &\quad \left. \dots \frac{\partial c(\boldsymbol{x},\boldsymbol{\mu}_z)}{\partial z_j} \mathrm{cov}(z_i, z_j) \right).\end{aligned} \tag{48}$$

In order to reduce the computational costs to a minimum, the chain rule is applied and the partial derivatives with respect to $\boldsymbol{z}$ are replaced inside the double sum by Eq. (34). In doing so, Eq. (48) reads

$$\begin{aligned}\frac{\partial \sigma_{\mathrm{c}}^{\mathrm{FOSM}}}{\partial \varphi_e} &= \frac{1}{2\sigma_{\mathrm{c}}^{\mathrm{FOSM}}} \left(\sum_{i=1}^{2n_{\mathrm{con}}} \sum_{j=1}^{2n_{\mathrm{con}}} \mathrm{cov}(z_i, z_j) \right. \\ &\quad \dots \frac{\partial c(\boldsymbol{x},\boldsymbol{\mu}_z)}{\partial z_j} \frac{\partial}{\partial \varphi_e} \left[-\boldsymbol{\zeta}^{\mathrm{T}} \left(\frac{\partial \boldsymbol{J}_{\mathrm{c}}(\boldsymbol{x}(\boldsymbol{\mu}_z))}{\partial z_i} \boldsymbol{x}(\boldsymbol{\mu}_z) \right. \right. \\ &\quad \left. \left. \dots - \frac{\partial \boldsymbol{r}_{\mathrm{c}}(\boldsymbol{\mu}_z)}{\partial z_i} \right) \right] + \mathrm{cov}(z_i, z_j) \frac{\partial c(\boldsymbol{x},\boldsymbol{\mu}_z)}{\partial z_i} \frac{\partial}{\partial \varphi_e} \left[\right. \\ &\quad \left. \left. \dots - \boldsymbol{\zeta}^{\mathrm{T}} \left(\frac{\partial \boldsymbol{J}_{\mathrm{c}}(\boldsymbol{x}(\boldsymbol{\mu}_z))}{\partial z_j} \boldsymbol{x}(\boldsymbol{\mu}_z) - \frac{\partial \boldsymbol{r}_{\mathrm{c}}(\boldsymbol{\mu}_z)}{\partial z_j} \right) \right] \right).\end{aligned} \tag{49}$$

The computation of $\frac{\partial \boldsymbol{\zeta}}{\partial \varphi_e}$ and $\frac{\partial \boldsymbol{x}}{\partial \varphi_e}$ are costly, which is why, two adjoint equations are needed. The variance approximation is extended by the arbitrary adjoint variables $\boldsymbol{\eta}$ and $\boldsymbol{\xi}$, that are multiplied with the equilibrium equations $\boldsymbol{h}_{\mathrm{c}}(\boldsymbol{x}(\boldsymbol{\mu}_z)) = \boldsymbol{0}$ and the adjoint Eq. (33)

$$\begin{aligned}\left(\tilde{\sigma}_{\mathrm{c}}^{\mathrm{FOSM}}\right)^2 &= \left(\sigma_{\mathrm{c}}^{\mathrm{FOSM}}\right)^2 - \boldsymbol{\eta}^{\mathrm{T}} \underbrace{\boldsymbol{h}_{\mathrm{c}}(\boldsymbol{x}(\boldsymbol{\mu}_z))}_{=\boldsymbol{0}} \\ &\quad \dots - \underbrace{\left(\boldsymbol{r}^{\mathrm{T}} - \boldsymbol{\zeta}^{\mathrm{T}} \boldsymbol{J}_{\mathrm{c}}(\boldsymbol{x}(\boldsymbol{\mu}_z))\right)}_{=\boldsymbol{0}^{\mathrm{T}}} \boldsymbol{\xi}.\end{aligned} \tag{50}$$

Next, Eq. (49) must be extended as well

$$\begin{aligned}\frac{\partial \tilde{\sigma}_{\mathrm{c}}^{\mathrm{FOSM}}}{\partial \varphi_e} &= \frac{1}{2\sigma_{\mathrm{c}}^{\mathrm{FOSM}}} \left[-\boldsymbol{\eta}^{\mathrm{T}} \frac{\partial \boldsymbol{h}_{\mathrm{c}}(\boldsymbol{x}(\boldsymbol{\mu}_z))}{\partial \varphi_e} - \right. \\ &\quad \dots \frac{\partial}{\partial \varphi_e} \left(\boldsymbol{r}^{\mathrm{T}} - \boldsymbol{\zeta}_i^{\mathrm{T}} \boldsymbol{J}_{\mathrm{c}}(\boldsymbol{x}(\boldsymbol{\mu}_z))\right) \boldsymbol{\xi} + \sum_{i=1}^{2n_{\mathrm{con}}} \sum_{j=1}^{2n_{\mathrm{con}}} \left(\right. \\ &\quad \dots \mathrm{cov}(z_i, z_j) \frac{\partial}{\partial \varphi_e} \left[-\boldsymbol{\zeta}^{\mathrm{T}} \left(\frac{\partial \boldsymbol{J}_{\mathrm{c}}(\boldsymbol{x}(\boldsymbol{\mu}_z))}{\partial z_i} \boldsymbol{x}(\boldsymbol{\mu}_z) \right. \right. \\ &\quad \left. \left. \dots - \frac{\partial \boldsymbol{r}_{\mathrm{c}}(\boldsymbol{\mu}_z)}{\partial z_i} \right) \right] + \frac{\partial c(\boldsymbol{x},\boldsymbol{\mu}_z)}{\partial z_j} \mathrm{cov}(z_i, z_j) \frac{\partial c(\boldsymbol{x},\boldsymbol{\mu}_z)}{\partial z_i} \\ &\quad \left. \left. \dots \frac{\partial}{\partial \varphi_e} \left[-\boldsymbol{\zeta}^{\mathrm{T}} \left(\frac{\partial \boldsymbol{J}_{\mathrm{c}}(\boldsymbol{x}(\boldsymbol{\mu}_z))}{\partial z_j} \boldsymbol{x}(\boldsymbol{\mu}_z) - \frac{\partial \boldsymbol{r}_{\mathrm{c}}(\boldsymbol{\mu}_z)}{\partial z_j} \right) \right] \right) \right].\end{aligned} \tag{51}$$

Note that, the following partial derivatives are zero

$$\begin{aligned}&\frac{\partial \boldsymbol{r}}{\partial \varphi_e} = \boldsymbol{0}, \quad \frac{\partial \boldsymbol{r}_{\mathrm{c}}}{\partial \varphi_e} = \boldsymbol{0}, \quad \frac{\partial^2 \boldsymbol{r}_{\mathrm{c}}}{\partial z_i \partial \varphi_e} = \boldsymbol{0} \\ &\text{and} \quad \frac{\partial^2 \boldsymbol{J}_{\mathrm{c}}(\boldsymbol{x}(\boldsymbol{\mu}_z)}{\partial z_i \partial \varphi_e} = \begin{bmatrix} \boldsymbol{0} & \boldsymbol{0} \\ \boldsymbol{0} & \boldsymbol{0} \end{bmatrix}.\end{aligned} \tag{52}$$

As a result, the derivative of Eq. (51) simplifies to

$$\frac{\partial \sigma_c^{\mathrm{FOSM}}}{\partial \varphi_e} = \frac{\partial \tilde{\sigma}_c^{\mathrm{FOSM}}}{\partial \varphi_e} = \frac{1}{2\sigma_c^{\mathrm{FOSM}}} \Bigg[-\boldsymbol{\eta}^{\mathrm{T}} \dots \frac{\partial \boldsymbol{J}_c(\boldsymbol{x}(\boldsymbol{\mu}_z))}{\partial \varphi_e} \boldsymbol{x}(\boldsymbol{\mu}_z) + \boldsymbol{\zeta}^{\mathrm{T}} \frac{\partial \boldsymbol{J}_c(\boldsymbol{x}(\boldsymbol{\mu}_z))}{\partial \varphi_e} \boldsymbol{\xi} \Bigg]. \tag{53}$$

Thereby, the following adjoint equations must be satisfied

$$\begin{aligned} \mathbf{0} = -\sum_{i=1}^{2n_{\mathrm{con}}} \sum_{j=1}^{2n_{\mathrm{con}}} \Bigg[\mathrm{cov}(z_i, z_j) \boldsymbol{\zeta}^{\mathrm{T}} \Bigg(\frac{\partial c(\boldsymbol{x}, \boldsymbol{\mu}_z)}{\partial z_j} \\ \dots \frac{\partial \boldsymbol{J}_c(\boldsymbol{x}(\boldsymbol{\mu}_z))}{\partial z_i} + \frac{\partial c(\boldsymbol{x}, \boldsymbol{\mu}_z)}{\partial z_i} \frac{\partial \boldsymbol{J}_c(\boldsymbol{x}(\boldsymbol{\mu}_z))}{\partial z_j} \Bigg) \Bigg] \\ \dots - \boldsymbol{\eta}^{\mathrm{T}} \boldsymbol{J}_c(\boldsymbol{x}(\boldsymbol{\mu}_z)), \end{aligned} \tag{54}$$

$$\begin{aligned} 0 = \sum_{i=1}^{2n\mathrm{con}} \sum_{i=1}^{2n\mathrm{con}} \Bigg[\mathrm{cov}(z_i, z_j) \Bigg(\frac{\partial c(\boldsymbol{x}, \boldsymbol{\mu} z)}{\partial z_j} \Bigg[\frac{\partial \boldsymbol{J}_c(\boldsymbol{x}(\boldsymbol{\mu} z)}{\partial z_i} \\ \dots \boldsymbol{x}(\boldsymbol{\mu} z) - \frac{\partial \boldsymbol{r}_c}{\partial z_i} \Bigg] + \frac{\partial c(\boldsymbol{x}, \boldsymbol{\mu} z)}{\partial z_i} \Bigg(\frac{\partial \boldsymbol{J}_c(\boldsymbol{x}(\boldsymbol{\mu} z)}{\partial z_j} \\ \dots \boldsymbol{x}(\boldsymbol{\mu} z) - \frac{\partial \boldsymbol{r}_c}{\partial z_i} \Bigg) \Bigg) \Bigg] + \boldsymbol{J}_c(\boldsymbol{x}(\boldsymbol{\mu} z) \boldsymbol{\xi}. \end{aligned} \tag{55}$$

Finally, the derivative of the objective with respect to the design variables $\boldsymbol{\varphi}$ is defined as the sum of Eqs. (46) and (53). It reads

$$\begin{aligned} \frac{\partial \left(\mu_c^{\mathrm{FOSM}} + \kappa \sigma_c^{\mathrm{FOSM}} \right)}{\partial \varphi_e} = \zeta^{\mathrm{T}} \Bigg(\frac{\partial \boldsymbol{J}_c(\boldsymbol{x}(\boldsymbol{\mu} z))}{\partial \varphi_e} \\ \dots \boldsymbol{x}(\boldsymbol{\mu} z)) + \frac{\kappa}{2\sigma_c^{\mathrm{FOSM}}} \Bigg[-\eta^{\mathrm{T}} \frac{\partial \boldsymbol{J}_c(\boldsymbol{x}(\boldsymbol{\mu} z)}{\partial \varphi_e} \boldsymbol{x}(\boldsymbol{\mu} z) \\ \dots + \zeta^{\mathrm{T}} \frac{\partial \boldsymbol{J}_c(\boldsymbol{x}(\boldsymbol{\mu} z))}{\partial \varphi_e} \boldsymbol{\xi} \Bigg], \end{aligned} \tag{56}$$

where the adjoint Eqs. (33), (54), and (55) must be satisfied.

4.3 Gradient of the Volume Constraint

Next to the objective, the gradient of the volume constraint is needed. The constraint is introduced in Eq. (27) and its derivative with respect to the density of the e-th element reads

$$\frac{\partial V(\boldsymbol{\varphi})}{\partial \varphi_e} = V_e, \tag{57}$$

where the volume of the e-th undeformed element is V_e. The gradient of the volume constraint with respect to the design variables is independent of the design variables and therefore constant.

4.4 Accuracy of the first-order second-moment method

The fist-order second-moment method is based on a first order Taylor series and therefore, the accuracy of the approach depends on the impact of the random parameters on the objective of the optimization problem. In consequence, if the compliance depends linearly on the random geometries z_{g} and the random friction coefficients $z_{\hat{\mu}}$, FOSM is as accurate as possible for the non-linear and non-smooth contact problem. This implies, that higher order derivatives of the compliance with respect to the random parameters are zero.

Since the scattering of the random gaps z_{g} and the random friction coefficients $z_{\hat{\mu}}$ are assumed to be independent of each other, the impact of both is derived separately.

4.4.1 Accuracy for the random contact geometry

The second order derivative with respect to the random contact gap z_{g}^j is derived from Eq. (31), where the arbitrary adjoint $\boldsymbol{\zeta}$ was introduced. It reads

$$\frac{\partial^2 c}{\partial z_{\mathrm{g}}^i \partial z_{\mathrm{g}}^j} = \boldsymbol{r}^{\mathrm{T}} \frac{\partial^2 \boldsymbol{x}}{\partial z_{\mathrm{g}}^i \partial z_{\mathrm{g}}^j} - \boldsymbol{\zeta}^{\mathrm{T}} \frac{\partial^2 \boldsymbol{h}(\boldsymbol{x})}{\partial z_{\mathrm{g}}^i \partial z_{\mathrm{g}}^j}, \tag{58}$$

since the vector $\boldsymbol{r}$ does not depend on z_{g}. Further, Eq. (58) can be rewritten as

$$\frac{\partial^2 c}{\partial z_{\mathrm{g}}^i \partial z_{\mathrm{g}}^j} = \left(\boldsymbol{r}^{\mathrm{T}} - \boldsymbol{\zeta}^{\mathrm{T}} \boldsymbol{J}_{\mathrm{c}} \right) \frac{\partial^2 \boldsymbol{x}}{\partial z_{\mathrm{g}}^i \partial z_{\mathrm{g}}^j} + \boldsymbol{\zeta}^{\mathrm{T}} \frac{\partial^2 \boldsymbol{r}_{\mathrm{c}}}{\partial z_{\mathrm{g}}^i \partial z_{\mathrm{g}}^j}, \tag{59}$$

where the adjoint vector $\boldsymbol{\zeta}$ is once again chosen such that

$$\left(\boldsymbol{r}^{\mathrm{T}} - \boldsymbol{\zeta}^{\mathrm{T}} \boldsymbol{J}_{\mathrm{c}} \right) = \mathbf{0}. \tag{60}$$

In consequence, the second order derivative of the compliance with respect to the random contact gap is

$$\frac{\partial^2 c}{\partial z_{\mathrm{g}}^i \partial z_{\mathrm{g}}^j} = \boldsymbol{\zeta}^{\mathrm{T}} \frac{\partial^2 \boldsymbol{r}_{\mathrm{c}}}{\partial z_{\mathrm{g}}^i \partial z_{\mathrm{g}}^j} = 0 \quad , \text{since} \quad \frac{\partial^2 \boldsymbol{r}_{\mathrm{c}}}{\partial z_{\mathrm{g}}^i \partial z_{\mathrm{g}}^j} = 0. \tag{61}$$

Hence, if the contact gaps scatter randomly, higher order concepts will not increase the accuracy in comparison to the first-order second-moment method. Note that, this result implies, that the mean and the variance computed by FOSM are the actual mean and variance of the system, if the equilibrium equations would be smooth. However, the unilateral contact-constraints are non-smooth and therefore the equilibrium Eq. (17) is non-smooth as well, so that FOSM does not compute the actual mean and variance. The impact of this non-smooth behavior is discussed in the numerical

examples, where FOSM is compared to Monte Carlo simulations.

4.4.2 Accuracy for the random friction coefficients

The second order derivative with respect to the random friction coefficient $z^j_{\hat{\mu}}$ is derived from Eq. (31) as well, where the arbitrary adjoint $\boldsymbol{\zeta}$ was introduced. It is

$$\frac{\partial^2 c(\boldsymbol{x},\boldsymbol{\mu}_z)}{\partial z^i_{\hat{\mu}} \partial z^j_{\hat{\mu}}} = \boldsymbol{r}^{\mathrm{T}} \frac{\partial^2 \boldsymbol{x}(\boldsymbol{\mu}_z)}{\partial z^i_{\hat{\mu}} \partial z^j_{\hat{\mu}}} - \boldsymbol{\zeta}^{\mathrm{T}} \frac{\partial^2 \boldsymbol{h}(\boldsymbol{x}(\boldsymbol{\mu}_z))}{\partial z^i_{\hat{\mu}} \partial z^j_{\hat{\mu}}}, \tag{62}$$

since the vector $\boldsymbol{r}$ does not depend on $z_{\hat{\mu}}$. Further, the vector $\boldsymbol{r}_{\mathrm{c}}(\boldsymbol{\mu}_z)$ is independent of $z_{\hat{\mu}}$, but the partial derivate of the contact Jacobian $\dfrac{\partial \boldsymbol{J}_{\mathrm{c}}(\boldsymbol{x}(\boldsymbol{\mu}_z))}{\partial z_{\hat{\mu}}}$ is constant and was introduced in Eqs. (35) and (36). Consequentially, Eq. (62) simplifies to

$$\begin{aligned}\frac{\partial^2 c(\boldsymbol{x},\boldsymbol{\mu}_z)}{\partial z^i_{\hat{\mu}} \partial z^j_{\hat{\mu}}} &= \boldsymbol{r}^{\mathrm{T}} \frac{\partial^2 \boldsymbol{x}(\boldsymbol{\mu}_z)}{\partial z^i_{\hat{\mu}} \partial z^j_{\hat{\mu}}} - \boldsymbol{\zeta}^{\mathrm{T}} \Bigg(\frac{\partial \boldsymbol{J}_{\mathrm{c}}(\boldsymbol{x}(\boldsymbol{\mu}_z))}{\partial z^i_{\hat{\mu}}} \\ &\quad \cdots \frac{\partial \boldsymbol{x}(\boldsymbol{\mu}_z)}{\partial z^j_{\hat{\mu}}} + \frac{\partial \boldsymbol{J}_{\mathrm{c}}(\boldsymbol{x}(\boldsymbol{\mu}_z))}{\partial z^j_{\hat{\mu}}} \frac{\partial \boldsymbol{x}(\boldsymbol{\mu}_z)}{\partial z^i_{\hat{\mu}}} \\ &\quad \cdots + \boldsymbol{J}_{\mathrm{c}}(\boldsymbol{x}(\boldsymbol{\mu}_z)) \frac{\partial^2 \boldsymbol{x}(\boldsymbol{\mu}_z)}{\partial z^i_{\hat{\mu}} \partial z^j_{\hat{\mu}}} \Bigg)\end{aligned} \tag{63}$$

$$\begin{aligned}&= \left(\boldsymbol{r}^{\mathrm{T}} - \boldsymbol{\zeta}^{\mathrm{T}} \boldsymbol{J}_{\mathrm{c}}(\boldsymbol{x}(\boldsymbol{\mu}_z))\right) \frac{\partial^2 \boldsymbol{x}(\boldsymbol{\mu}_z)}{\partial z^i_{\hat{\mu}} \partial z^j_{\hat{\mu}}} - \boldsymbol{\zeta}^{\mathrm{T}} \Bigg(\frac{\partial \boldsymbol{x}(\boldsymbol{\mu}_z)}{\partial z^j_{\hat{\mu}}} \\ &\cdots \frac{\partial \boldsymbol{J}_{\mathrm{c}}(\boldsymbol{x}(\boldsymbol{\mu}_z))}{\partial z^i_{\hat{\mu}}} + \frac{\partial \boldsymbol{J}_{\mathrm{c}}(\boldsymbol{x}(\boldsymbol{\mu}_z))}{\partial z^j_{\hat{\mu}}} \frac{\partial \boldsymbol{x}(\boldsymbol{\mu}_z)}{\partial z^i_{\hat{\mu}}} \Bigg).\end{aligned} \tag{64}$$

Eq. (64) shows, that the second order derivative of the compliance does not vanish, so that higher order approximations will increase the accuracy of the approximation of the mean and the variance. As always, higher order approximations result in higher numerical costs, since more equations must be solved.

5 Numerical Examples

The introduced robust compliance optimization is applied to 2D and 3D examples of Strömberg and Klarbring (2010). First, 2D examples are considered and the accuracy of the robust optimization as well as the convergence are analyzed. Next, the algorithms are applied to 3D examples.

5.1 2D Benchmark of Strömberg and Klarbring

The benchmark example of Strömberg and Klarbring (2010) is shown in Fig. 3. The design domain represents a lug which is unilaterally constrained by a rigid pin. Additionally, a sliding bearing in the lower left corner is considered and the domain is loaded in the lower right corner. The applied loads are either in horizontal or vertical direction and the design domain is discretized by 4444 finite elements, which results in 50 contact nodes at the rigid pin. The considered linear-elastic material is characterized by a Young's modulus of 210 GPa and a Poisson's ratio of 0.3. Further, the truncation radius of the used sensitivity filter , see Sigmund (2007), is 10 mm and the volume fraction is 0.5.

At first, the geometry of the rigid pin scatters and in Sect. 5.1.2 the friction coefficients scatter.

5.1.1 Random Contact Geometry

The scattering of the random parameters is described by the covariance matrix of Eq. (29) including the exponential correlation function of Eq. (28). The correlation length is set to $l_c = 25$ mm and the contact gaps are assumed to be normal distributed with zero mean. The benchmark example was introduced without friction and therefore, friction is not considered here.

The robust optimization problem for the benchmark example considering all four load cases $f_x = \pm 1000$ N and $f_y = \pm 1000$ N reads

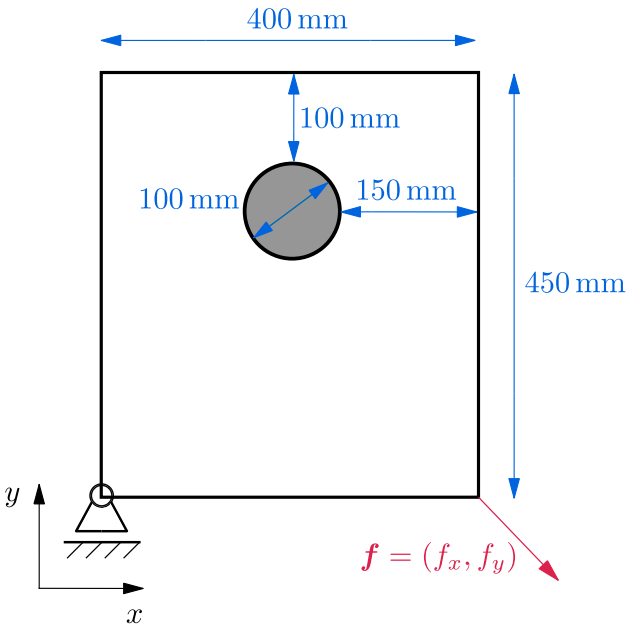

Fig. 3 The design domain of the 2D benchmark example of Strömberg and Klarbring (2010)

$$\min_{\boldsymbol{\varphi}} \sum_{i=1}^{n=4} \left[\frac{1}{4} \left(\mu_c(\boldsymbol{\varphi})_i + 3\sigma_c(\boldsymbol{\varphi})_i \right) \right]$$
$$\text{s.t.} \begin{cases} \boldsymbol{h}_c(\boldsymbol{\varphi}, \boldsymbol{x})_i = \mathbf{0}, \\ V(\boldsymbol{\varphi}) - V_0 \leq 0, \\ \mathbf{0} \leq \boldsymbol{\varphi} \leq \mathbf{1}. \end{cases} \tag{65}$$

The scattering of the contact gaps is based on manufacturing tolerances with respect to the *DIN EN ISO 286-1*. In doing so, the assumed random scattering of the rigid pin is chosen in the range of component fits ranging from IT5 to IT11. The scattering of $\sigma(z_g^i) = 10\,\mu m$ corresponds to an International Tolerance Grade of IT7, whereas $\sigma(z_g^i) = 25\,\mu m$ corresponds to IT9 and $\sigma(z_g^i) = 50\,\mu m$ corresponds to IT11. The convergence of the method is shown in Fig. 4 and the robust as well as the deterministic optimization converge as expected. If larger scatterings of the contact geometry are considered, higher objective values are obtained, which is expected. This can also be seen in Table 1, where the final average mean and the final standard deviation of the optimizations are listed. The optimized domains for the random contact geometry are shown in Fig. 5.

Figure 5a visualizes the reference solution for the deterministic optimization, without considering any contact geometry scattering, as it is proposed by Strömberg and Klarbring (2010). In contrast, Fig. 5b–d show the optimized designs for the robust optimization using FOSM. Here, the optimized designs are computed considering the random scattering of the geometry, which is characterized by the standard deviation $\sigma(z_g^i)$. The results reveal that a small scattering of the geometry results in the same optimized design Fig. 5b, while larger scatterings lead to a wider support in the left and right diagonal strut at the cost of a splitting the struts. Furthermore, the material at the bottom of the rigid pin vanishes for large scatterings (see Fig. 5d), which increases the local deformability of the component at the pin. This crack-like topology can be reduced using density filtering, see Bruns and Tortorelli (2001), instead of Sigmund's Filter. The optimized design using density filtering is shown in Fig. 6a and the combination of density and projection filtering is shown in Fig. 6b, where the latter outperforms the other two filtering techniques. Applying these filtering techniques to the smaller scatterings of Fig. 5b and c results only in minor changes. Nonetheless, Sigmund's filter is used in this work, since it is used in the deterministic benchmark example Strömberg and Klarbring (2010).

The average compliance and the average standard deviations with respect to all four load cases

$$\mu_c = \frac{1}{4} \sum_{i=1}^{n=4} \mu_c(\boldsymbol{\varphi})_i \quad \text{and} \quad \sigma_c = \frac{1}{4} \sum_{i=1}^{n=4} \sigma_c(\boldsymbol{\varphi})_i, \tag{66}$$

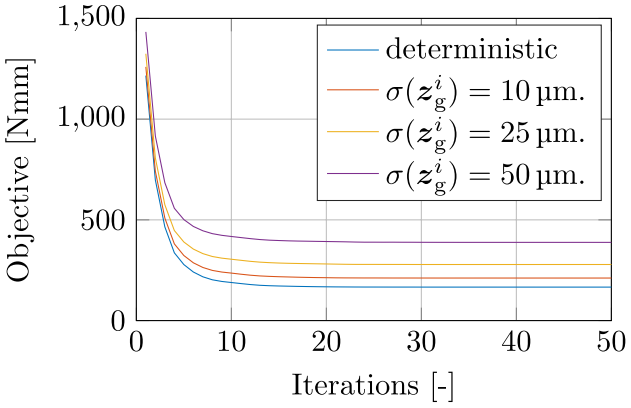

Fig. 4 Convergence of the optimization problem Eq. (65) for different standard deviations $\sigma(z_g^i)$ of the random contact gaps

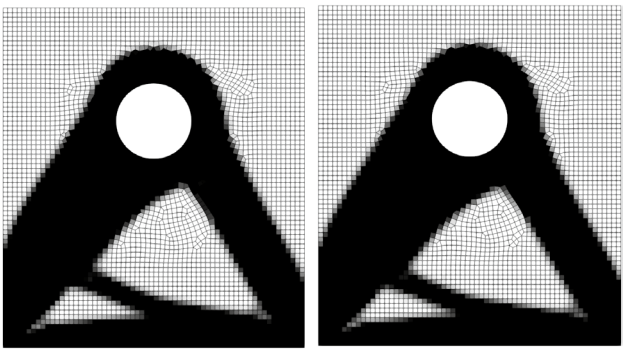

(a) Deterministic optimization [18].

(b) Robust opt. $\sigma(z_g^i) = 10\,\mu m$.

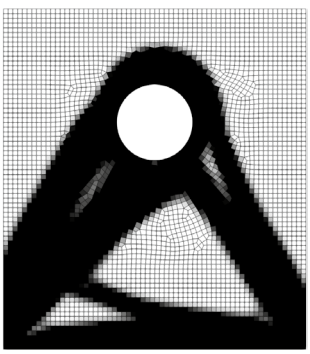

(c) Robust opt. $\sigma(z_g^i) = 25\,\mu m$.

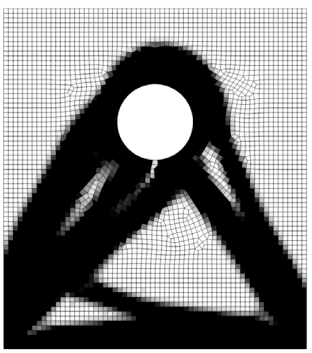

(d) Robust opt. $\sigma(z_g^i) = 50\,\mu m$.

Fig. 5 Comparison of the optimized designs using deterministic and robust optimization for different standard deviations $\sigma(z_g^i)$ of the random contact gaps after 50 iterations

are shown in Table 1. For the deterministic optimization, the expected compliance is the lowest. However, the standard deviation of the optimized design decreases using the robust optimization approach. Looking at $\sigma(z_g^i) = 25\,\mu m$, the aver-

age compliance increases by 0.6%, while the average standard deviation decreases by 1.5%. If a random scattering of $\sigma(z_g^i) = 50\,\mu m$ is considered, the average compliance increases by 2.1%, while the average standard deviation decreases by 3.2%. Consequentially, the presented robust optimization approach reduces the standard deviation at the cost of increasing the mean compliance of the component. This is to be expected since the robust objective Eq. (27) considers the mean and the standard deviation, where as the deterministic optimization does only consider the actual compliance in an ideal setup.

All simulations are performed on a standard workstation and all performed optimizations terminate after 50 iterations. In doing so, the deterministic optimization takes 254 s, while the robust cases takes 4 to 5 times longer. More precisely, the robust optimization based on $\sigma(z_g^i) = 10\,\mu m$ takes 1011 s, $\sigma(z_g^i) = 25\,\mu m$ takes 1226 s and $\sigma(z_g^i) = 50\,\mu m$ takes 1235 s.

Last, the accuracy of the first-order second-moment is analyzed using Monte Carlo simulations with 10,000 random samples. In Sect. 4.4 it is shown, that the FOSM approach is accurate, if the system equations of the contact problem do not change. More precisely, the mean and variance computed by the FOSM are exact if and only if the contact surface does not change, for any non-perfect contact geometry. This is unlikely in practice and in Monte Carlo simulations. In consequence, the contact surface might adapt to the imperfect geometry, which can lead to switching contact conditions in comparison to the ideal geometry. Some nodes at the contact surface might come into contact or might lose contact with the contact surface. The resulting average compliance and the standard deviation considering all four load cases are shown in Table 2. It turns out, that

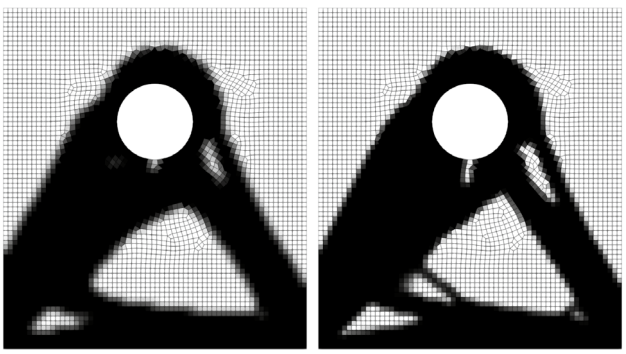

(a) Density filter. $\mu_c = 169.57\,,\ \sigma_c = 73.55\,.$

(b) Density and projection filter. $\mu_c = 168.90\,,\ \sigma_c = 72.82\,.$

Fig. 6 The impact of different filtering techniques in comparison to Fig. 5d

Table 1 Average compliance and standard deviation of the optimized designs approximated by FOSM for different geometry scatters $\sigma(z_g^i)$. (Fig. 5a—deterministic design, Fig. 5b–d—robust design)

$\sigma(z_g^i)$	det. μ_c	det. σ_c	rob. μ_c	rob. σ_c
10 (Fig. 5a & 5b)	166.18	15.05	166.25	14.97
25 (Fig. 5a & 5c)	166.18	37.63	167.20	37.06
50 (Fig. 5a & 5d)	166.18	75.25	169.67	72.87

the FOSM approach overestimates the average compliance of the optimized designs by up to 3.3% for the deterministic optimized design and by up to 3.5% for the robust designs. Looking into the average standard deviations, very good results are obtained for the smaller scattering of the random contact geometry. However, if larger scattering is considered, the standard deviation of FOSM overestimates the standard deviation by up to 31.2%. Nonetheless, the standard deviations obtained by FOSM are still predicting that the deterministic design is more sensitive than the robust design.

For the presented contact problem, FOSM overestimates the results obtained by the Monte Carlo simulations. This observation might be explained with the principal of minimum potential in the Finite Element Method. The contact surface must adapt to the imperfect contact geometry, which results in a smaller potential than neglecting these adaptions. The adapting contact surface is not considered using FOSM, so that - considering reasonable scattering - FOSM will approximate higher values for the mean and variance. If the scattering of the contact geometry becomes too large, the non-smoothness of the contact problem dominates. Thus, a linear method such as FOSM might not provide reasonable approximations anymore. In this case, Monte Carlo simulations are challenging as well, since solving the non-linear and non-smooth contact problem for highly irregular deviations from the ideal shape of the contact support becomes numerically more and more challenging. Additionally, assumptions such as linear-elasticity must be questioned as well, since the contact support is modeled as rigid body. Therefore, only the design domain can adapt to the deviations of the contact support yielding large deformations, if large scattering is considered. Whether this point is reached depends strongly on the model parameters. Thus, robust

Table 2 Average compliance and standard deviation of the optimized designs based on 10,000 Monte Carlo Samples for different geometry scatters $\sigma(z_g^i)$. (Fig. 5a - deterministic design, Fig. 5b to d - robust design)

$\sigma(z_g^i)$	det. μ_c	det. σ_c	rob. μ_c	rob. σ_c
10 (Fig. 5a & 5b)	162.07	14.89	162.15	14.90
25 (Fig. 5a & 5c)	161.11	34.93	161.78	31.33
50 (Fig. 5a & 5d)	160.65	57.33	163.74	55.77

optimization is here only applied for standard manufacturing tolerances.

5.1.2 Random Friction Coefficients

The scattering of the random friction coefficients is described by the covariance matrix of Eq. (29) including the exponential correlation function of Eq. (28). The correlation length is set to $l_c = 25$ mm and the friction coefficients are assumed to be uniformly distributed between 0.15 and 0.25. In order to apply global sliding friction, the rigid pin of the benchmark example is rotating in clockwise (cw) or counterclockwise (ccw) direction. The same four load cases are considered, but the weighting factor is increased to 30. The optimization terminates after 50 iterations and the optimization problem reads

$$\min_{\boldsymbol{\varphi}} \sum_{i=1}^{n=4} \left[\frac{1}{4} \left(\mu_c(\boldsymbol{\varphi})_i + 30\sigma_c(\boldsymbol{\varphi})_i \right) \right] \quad \text{s.t.} \begin{cases} \boldsymbol{h}_c(\boldsymbol{\varphi}, \boldsymbol{x})_i = \mathbf{0}, \\ V(\boldsymbol{\varphi}) - V_0 \leq 0, \\ \mathbf{0} \leq \boldsymbol{\varphi} \leq \mathbf{1}. \end{cases} \tag{67}$$

The convergence of all optimizations are shown in Fig. 7 and the optimized designs are shown in Fig. 8. Also for the random friction coefficients convergence is observed, but it is a lot more difficult to distinguish between the deterministic and robust optimization. This is due to the fact, that the standard deviation of the compliance $\sigma_c(\boldsymbol{\varphi})_i$ is smaller than 1% of the mean $\mu_c(\boldsymbol{\varphi})_i$. Further, the direction of the rotation of the pin has a significant impact on the objective.

Even though the impact of the random friction coefficients on the compliance is small, different designs are obtained using the proposed robust optimization approach. Looking at the designs for the clockwise rotating pin (Fig. 8a and b), only minor changes of the topology around the contact support and the positioning of the small strut are observed. If the pin rotates counterclockwise (Fig. 8c and d), the right strut splits up. Additionally, minor changes of the topology around the contact support and the positioning of the small strut are observed again.

The resulting average mean and the average standard deviation approximated by FOSM are listed in Table 3. Here, the robust designs for the clockwise and counterclockwise rotating pin reduce the standard deviation by 8–9%, while the average compliance increases by less than 1%. In consequence, a less sensitive and therefore more robust design is found. However, also the deterministic design is not very sensitive against the scattering friction coefficients.

Last, the accuracy of the derived method is analyzed using Monte Carlo simulations with 10,000 samples. It is shown

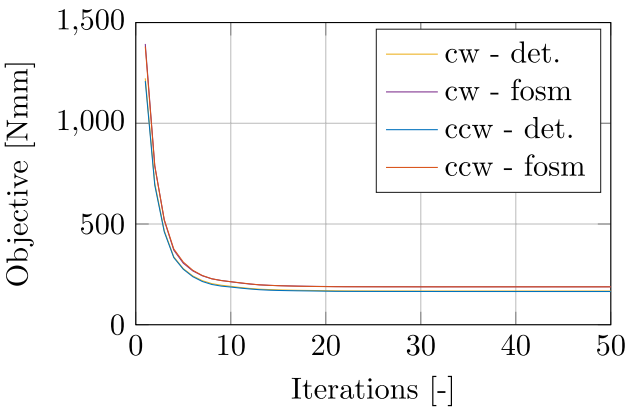

Fig. 7 Convergence of the optimization problem Eq. (67) considering random friction coefficients with a clockwise (cw) or counterclockwise (ccw) rotating pin

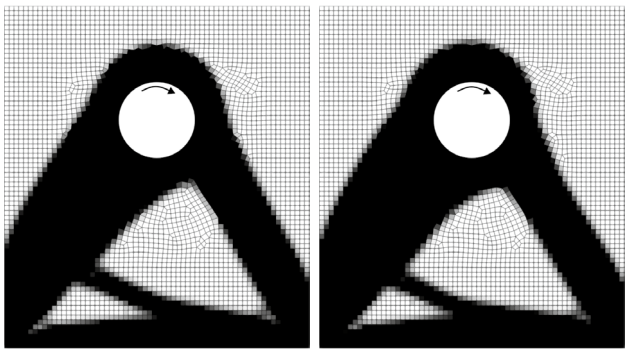

(a) Deterministic optimization with clockwise rotation.

(b) Robust optimization with clockwise rotation.

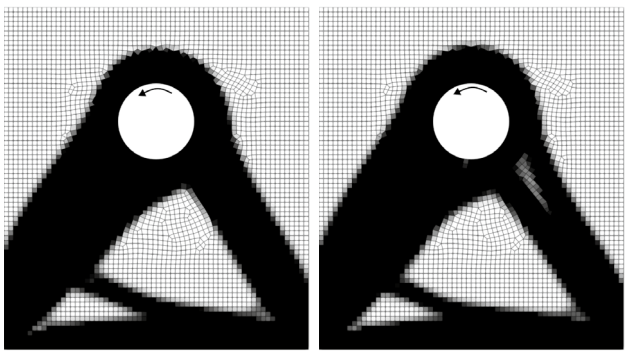

(c) Deterministic optimization with counterclockwise rotation.

(d) Robust optimization with counterclockwise rotation.

Fig. 8 Comparison of the optimized designs using deterministic and robust optimization with a rotating pin considering random friction coefficients after 50 iterations

Table 3 Average compliance and standard deviation of the optimized designs based on FOSM for a uniformly scattering friction coefficient $\hat{\mu} \in [0.15, 0.25]$ and a clockwise (cw) or counterclockwise (ccw) rotating pin

Rotation	det. μ_c	det. σ_c	rob. μ_c	rob. σ_c
cw (Fig. 8a & 8b)	167.18	0.73	168.10	0.67
ccw (Fig. 8c & 8d)	164.90	0.80	166.09	0.73

Table 4 Average compliance and standard deviation of the optimized designs based on 10,000 Monte Carlo Samples for a uniformly scattering friction coefficient $\hat{\mu} \in [0.15, 0.25]$ and a clockwise (cw) or counterclockwise (ccw) rotating pin

Rotation	det. μ_c	det. σ_c	rob. μ_c	rob. σ_c
cw (Fig. 8a & 8b)	167.16	0.72	168.10	0.67
ccw (Fig. 8c & 8d)	164.89	0.80	166.06	0.74

in Sect. 4.4, that the compliance does not linearly depend on the friction coefficients. In consequence, FOSM will not be exact and higher order methods will increase the accuracy. The results of Table 4 reveal a very good agreement with the results of Table 3. Hence, FOSM is sufficient to model the random friction coefficients in the presented example.

5.2 3D benchmark Strömberg and Klarbring

The presented robust framework is extended to the 3D problems of Strömberg and Klarbring (2010). The design domain of Fig. 3 is extruded 200 mm in z-direction and only the load case in negative y-direction is considered. The domain is discretized into 138,219 tetrahedral finite elements and 1650 contact nodes. The material parameters are not modified and 100 iterations are performed. All computation are performed on a standard workstation.

5.2.1 Random contact geometry

In doing so, the weighting factor is set to $\kappa = 0.05$ and the standard deviation of the scattering of the contact geometry is set to $\sigma(z_g^i) = 25\,\mu m$.

The deterministic design is shown in Fig. 9a and b, whereas the robust design is shown in Fig. 9c and d. One can see, that the two struts connecting the bearings and the contact super become thinner for the robust design, while more material is distributed at the top of the contact support. Furthermore, material is also placed inside the cutout at the contact support. These minor modifications lead to an increase of the average compliance μ_c by approx. 2%,

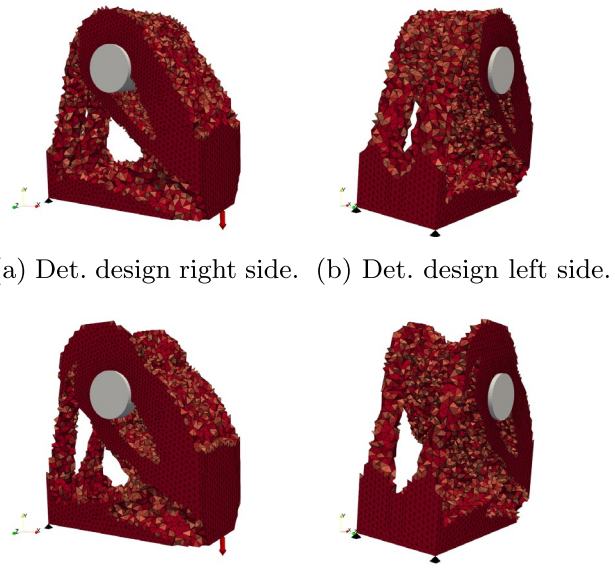

(a) Det. design right side. (b) Det. design left side.

(c) Rob. design right side. (d) Rob. design left side.

Fig. 9 Comparison of a deterministic optimized design (top) and robust optimized design (bottom) based on contact-constrained topology optimization

while the standard deviation σ_c is reduced by approx. 11% for the robust optimized design. These values are computed using FOSM, since Monte Carlo simulations are very expensive for 3D examples.

5.2.2 Random friction coefficients

Next, the friction coefficients are considered to be uniformly distributed between 0.15 and 0.25. The weighting factor is set to $\kappa = 100$ and the pin is rotating in either clockwise or counterclockwise direction. The optimized designs based on a clockwise rotation are shown in Fig. 10, whereas the counterclockwise case is shown in Fig. 11. Further, the approximated mean and standard deviations for all optimized designs are shown in Table 5. For both rotation directions, the robust designs have different strut sizes and positioning in comparison to the deterministic design, while the overall appearance of the component is similar. The robust designs have a smaller standard deviation and are therefore more robust against scattering friction coefficients. Nevertheless, the absolute values of the standard deviations are very low for all designs, so that in this example the deterministic design also performs well. In general it turns out that this example is not very sensitive to the friction coefficient as well as the direction of rotation of the pin.

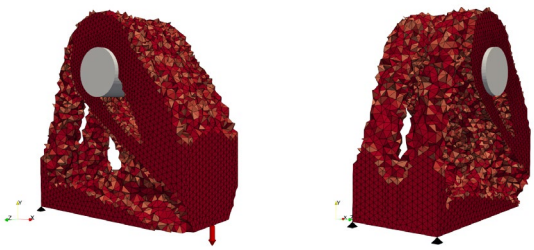

(a) Det. design right side. (b) Det. design left side.

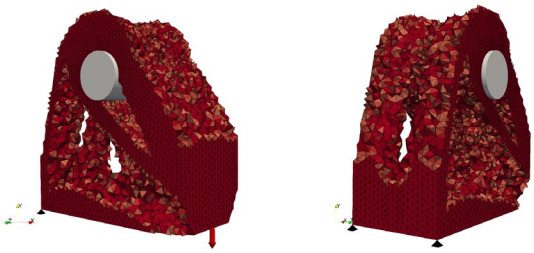

(c) Rob. design right side. (d) Rob. design left side.

Fig. 10 Comparison of a deterministic optimized design (top) and robust optimized design (bottom) based on contact-constrained topology optimization with a clockwise rotating pin

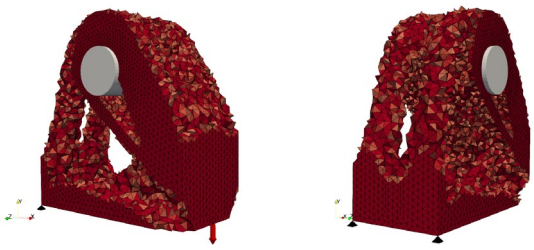

(a) Det. design right side. (b) Det. design left side.

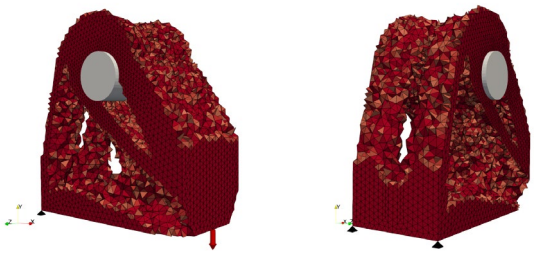

(c) Rob. design right side. (d) Rob. design left side.

Fig. 11 Comparison of a deterministic optimized design (top) and robust optimized design (bottom) based on contact-constrained topology optimization with a counterclockwise rotating pin

6 Conclusion

In this paper, the general framework for contact-constrained topology optimization of linear-elastic structures is extended to a robust design optimization problem. In doing so, the first-order second-moment method is used to approximate the mean and the standard deviation of the compliance with respect to the uncertain contact geometries and friction coefficients. It is shown, that the accuracy of the first-order second-moment method is sufficient even though a non-linear contact problem is considered. The optimized designs adapt to the robust optimization problem and less sensitive design are obtained. However, the changes in the design domain do only lead to decrease of the standard deviation by a few percent, which is to be expected since only realistic scatterings in the range of manufacturing tolerances are considered. Finally, the performance of the method is most efficient, so that also 3D applications can be computed.

Table 5 Compliance and standard deviation of the optimized designs based on FOSM for a uniformly scattering friction coefficient $\hat{\mu} \in [0.15, 0.25]$ and a clockwise (cw) or counterclockwise (ccw) rotating pin

Rotation	det. μ_c	det. σ_c	rob. μ_c	rob. σ_c
cw (Fig. 10)	1.3112	0.0008	1.3329	0.0004
ccw (Fig. 11)	1.2714	0.0010	1.2819	0.0007

Funding Open Access funding enabled and organized by Projekt DEAL. The current work is a part of the research training group "Simulation-Based Design Optimization of Dynamic Systems Under Uncertainties" (SENSUS) funded by the state of Hamburg within the Landesforschungsförderung under project number LFF-GK11.

Declarations

Conflict of interest On behalf of all authors, the corresponding author states that there is no conflict of interest.

Replication of results The used in-house Toolbox TOptiMuM cannot be published at this time. Nonetheless, all needed parameters to recompute the results are mentioned in the work.

References

Bruns TE, Tortorelli DA (2001) Topology optimization of non-linear elastic structures and compliant mechanisms. Comput Methods Appl Mech Eng 190(26–27):3443–3459. https://doi.org/10.1016/S0045-7825(00)00278-4

Cornell CA (1969) Structural safety specifications based on second-moment reliability analysis. IABSE Rep Work Commiss 4:235–245

Facchinei F, Jiang H, Qi L (1999) A smoothing method for mathematical programs with equilibrium constraints. Math Program 85:107–134. https://doi.org/10.1007/s10107990015a

Haldar A, Mahadevan S (1999) Probability, reliability, and statistical methods in engineering design, 1st edn. Wiley, New York

Jung HS, Cho S (2004) Reliability-based topology optimization of geometrically nonlinear structures with loading and material uncertainties. Finite Elem Anal Des 41(3):311–331. https://doi.org/10.1016/j.finel.2004.06.002

Keshavarzzadeh V, Fernandez F, Tortorelli DA (2017) Topology optimization under uncertainty via non-intrusive polynomial chaos expansion. Comput Methods Appl Mech Eng 318:120–147. https://doi.org/10.1016/j.cma.2017.01.019

Kranz M, Lüdeker JK, Kriegesmann B (2023) A generalized approach for robust topology optimization using the first-order second-moment method for arbitrary response functions. Struct Multidisc Optim 66(5):98. https://doi.org/10.1007/s00158-023-03540-w

Kriegesmann B, Lüdeker JK (2019) Robust compliance topology optimization using the first-order second-moment method. Struct Multidisc Optim 60:269–286. https://doi.org/10.1007/s00158-019-02216-8

Krüger JC, Kranz M, Schmidt T et al (2023) An efficient and non-intrusive approach for robust design optimization with the first-order second-moment method. Comput Methods Appl Mech Eng 414:116–136. https://doi.org/10.1016/j.cma.2023.116136

Lazarov BS, Schevenels M, Sigmund O (2012) Topology optimization with geometric uncertainties by perturbation techniques. Int J Numer Meth Eng 90(11):1321–1336. https://doi.org/10.1002/nme.3361

Maute K, Frangopol DM (2003) Reliability-based design of MEMS mechanisms by topology optimization. Comput Struct 81(8):813–824. https://doi.org/10.1016/S0045-7949(03)00008-7

Papoutsis-Kiachagias EM, Papadimitriou DI, Giannakoglou KC (2012) Robust design in aerodynamics using third-order sensitivity analysis based on discrete adjoint: application to quasi-1D flows. Int J Numer Meth Fluids 69(3):691–709. https://doi.org/10.1002/fld.2604

Schevenels M, Lazarov BS, Sigmund O (2011) Robust topology optimization accounting for spatially varying manufacturing errors. Comput Methods Appl Mech Eng 200(49–52):3613–3627. https://doi.org/10.1016/j.cma.2011.08.006

Schmidt T, Kriegesmann B, Seifried R (2022) Robust topology optimization of static systems with unilateral frictional contact. 8th Eur Congress Comput Methods Appl Sci Eng. https://doi.org/10.23967/eccomas.2022.237

Sigmund O (2007) Morphology-based black and white filters for topology optimization. Struct Multidiscip Optim 33:401–424. https://doi.org/10.1007/s00158-006-0087-x

Signorini A (1959) Questioni di elasticitá non linearizzata e semilinearizzata. Rendiconti di Matematica e delle sue Applicazioni 5:95–139

Steltner K, Pedersen CBW, Kriegesmann B (2022) Semi-intrusive approach for stiffness and strength topology optimization under uncertainty. Optim Eng. https://doi.org/10.1007/s11081-022-09770-z

Strömberg N, Klarbring A (2010) Topology optimization of structures in unilateral contact. Struct Multidisc Optim 41:57–64. https://doi.org/10.1007/s00158-009-0407-z

Svanberg K (1987) The method of moving asymptotes—a new method for structural optimizaion. Int J Numer Meth Eng 24:359–373

Zang T, Hemsch MJ, Hilburger MW, et al (2022) Needs and opportunities for uncertainty-based multidisciplinary design methods for aerospace vehicles. National Aeronautics and Space Administration Langley Research Center, NASA / TM-2002-211462 https://ntrs.nasa.gov/api/citations/20020063596/downloads/20020063596.pdf